ACS OMEGA

http://pubs.acs.org/journal/acsodf

Article

Simultaneous Observation of Visible Upconversion and Near-Infrared Downconversion in SrF_2:Nd^{3+}/Yb^{3+}/Er^{3+} Nanocrystals and Their Application for Detecting Metal Ions under Dual-Wavelength Excitation

Linxuan Wang,[¶] Weiqiang Yang,[¶] Liang Li, Shuai Hu, Maohui Yuan,[*] Zining Yang, Kai Han, Hongyan Wang,[*] and Xiaojun Xu

Cite This: *ACS Omega* 2022, 7, 27230−27238

Read Online

ACCESS | Metrics & More | Article Recommendations

ABSTRACT: In this work, a sequence of Nd^{3+}, Yb^{3+}, and Er^{3+} tridoped SrF_2 nanocrystals (NCs) is synthesized by a hydrothermal method. Both the efficient near-infrared downconversion luminescence (DCL) and visible upconversion luminescence (UCL) of the Er^{3+} and Nd^{3+} ions are simultaneously observed and systematically demonstrated under dual-wavelength excitation (808 and 980 nm continuous-wave lasers). Subsequently, the SrF_2:Nd^{3+}/Yb^{3+}/Er^{3+} (15/4/0.2 mol %) NCs with the strongest luminescence were utilized for detecting the metal ion concentrations under 808 nm excitation. The results reveal that both the UCL and DCL gradually decrease as the metal ion concentrations increase, and high sensitivity is obtained for Cu^{2+} ions with a detection limit of 0.22 nM (~650 nm) and 0.63 nM (~976 nm). In addition, these SrF_2:Nd^{3+}/Yb^{3+}/Er^{3+} NCs are further demonstrated to achieve a solid-state display under 980 nm excitation, exhibiting obvious "red" and "green" patterns by varying the doping rare earth ion concentrations.

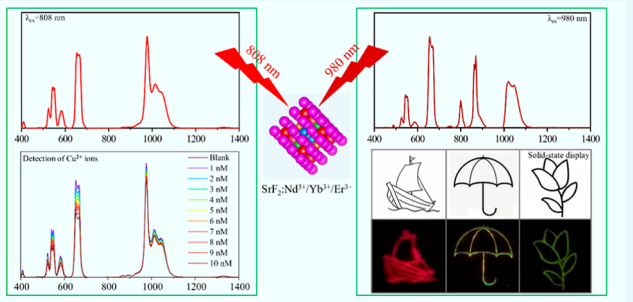

1. INTRODUCTION

In recent years, lanthanide-based upconversion nanocrystals (NCs) have become a research hotspot due to their significant advantages of a long fluorescence lifetime, narrow spectral width, large anti-Stokes shift, and low biotoxicity, which have been widely applied in temperature sensing,[1−3] biological therapy,[4] micro-/nanolasers,[5,6] solar cells,[7] and other aspects.[8,9] Generally, the so-called upconversion luminescence (UCL) process is an important approach for obtaining efficient luminescence emission. UCL refers to the conversion of lower-energy near-infrared (NIR) photons into relatively high-energy visible light through continuous photon absorption and energy-transfer (ET) processes based on the activator−sensitizer pairs. Popularly, Er^{3+} ions are used as activators emitting UCL, while the Yb^{3+} and Nd^{3+} ions act as sensitizers absorbing the excitation energy. Meanwhile, Er^{3+} and Nd^{3+} ions have abundant energy levels, whose main emission peaks range from visible to NIR regions. Compared to Yb^{3+} ions, Nd^{3+} ions have a larger absorption cross-section (1.2×10^{-19} cm^2) at 808 nm, which is about 10 times greater than that of Yb^{3+} ions at 980 nm.[10] In contrast, the water absorption coefficient of Nd^{3+} at 808 nm (0.02 cm^{-1}) is much lower than that of Yb^{3+} ions at 980 nm (0.48 cm^{-1}).[11] Thus, the Nd^{3+}-sensitized NCs have been widely utilized in biological issues or aqueous environment applications.

The host material has the most important role in generating both UCL and downconversion luminescence (DCL). In general, the low phonon energy of the host lattice is likely to reduce the nonradiative (NR) transition rates, thus promoting emission efficiency. Fluorides have a relatively low phonon energy (~350 cm^{-1}), as well as strong ionic properties, high transmittance in a wide spectral range from ultraviolet to infrared, high damage threshold, a low refractive index, easy storage, and other superior properties,[12,13] which have been utilized for doping rare earth ions and applied in many practical fields. Among these fluorides, SrF_2 is a promising host matrix with a cubic fluorspar structure and has attracted great attention.[14,15] Until now, many researchers have focused on investigating the UCL properties of NCs doped with either

Received: March 31, 2022
Accepted: July 14, 2022
Published: July 25, 2022

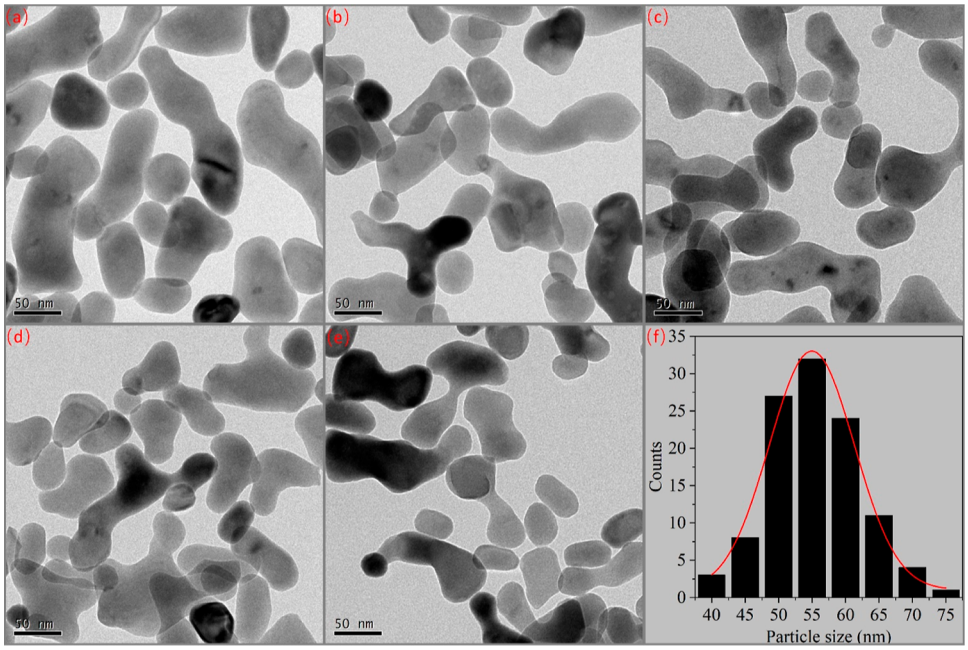

Figure 1. TEM images of SrF_2:Nd^{3+}/Yb^{3+}/Er^{3+}(15/4/x mol %) NCs. (a) x = 0.2, (b) x = 1, (c) x = 2, (d) x = 5, and (e) x = 10. (f) Particle size distribution of SrF_2:Nd^{3+}/Yb^{3+}/Er^{3+} (15/4/0.2 mol %) NCs.

Yb^{3+} or Nd^{3+} ions as sensitizers.[16] However, there are still few reports on the simultaneous realization of UCL and DCL generation in lanthanide-doped NCs, especially for tridoping with Nd^{3+}, Yb^{3+}, and Er^{3+} ions. This can achieve 980 and 808 nm dual-wavelength excitation and further promote their applications in both aqueous and nonaqueous environments.[17]

With the development of society and industry, human beings have higher requirements for water quality. How to quickly and accurately detect the amount of metal ions in a water environment is particularly important. The Cu^{2+} ion is an essential trace element in the human body, and it is needed to catalyze many biochemical processes in the body, but too much intake will lead to cancer and other diseases.[18,19] The maximum allowance of Cu^{2+} ions in drinking water, given by the World Health Organization (WHO), is ~31.5 μM.[20] At present, although the quantitative methods of metal ion detection include atomic absorption spectrometry, inductively coupled plasma mass spectrometry, or emission spectrometry, these methods are complicated and costly. In contrast, the optical sensors based on lanthanide-doped NCs are popularly employed to detect metal ions in the environment owing to their low cost and high sensitivity with fast response times.[21] Numerous reports have shown that lanthanide-doped NCs have good selectivity and high sensitivity for the detection of various metal ions.[22,23] Nevertheless, the present majority of sensors are operated by either singly detecting the UCL signal or under 980 nm excitation.

In this work, we have synthesized the Nd^{3+}, Yb^{3+}, and Er^{3+} tridoped SrF_2 NCs through a hydrothermal approach. The structure of these SrF_2 NCs was systematically characterized. Subsequently, we simultaneously investigated the visible UCL and NIR DCL properties in these NCs under the dual-wavelength excitation (both 808 and 980 nm). The dynamic properties, mechanism of population, and ET and emission processes are also demonstrated. Furthermore, the SrF_2:Nd^{3+}/Yb^{3+}/Er^{3+}(15/4/0.2 mol %) NCs were selected to act as high-sensitivity optical sensors for the detection of Cu^{2+} ions and other kinds of metal ions under 808 nm excitation. In addition, a potential solid-state display with different patterns is also demonstrated.

2. EXPERIMENTAL SECTION

2.1. Synthesis of Nanocrystals. The raw chemicals of $SrCl_2{\cdot}6H_2O$ (99.99%), $YbCl_3{\cdot}6H_2O$ (99.9%), $NdCl_3{\cdot}6H_2O$ (99.9%), $ErCl_3{\cdot}6H_2O$ (99.9%), $Na_3C_6H_5O_7$ (98%), and NH_4F (98%) were all purchased from Aladdin (China). The procedure of the synthesis of NCs is similar to that in our previous report.[24] Taking SrF_2:Nd^{3+}/Yb^{3+}/Er^{3+} (15/4/1 mol %) NCs as an example, 10 mL of solution of chloride salts (1.6 mmol $SrCl_2$, 0.3 mmol $NdCl_3$, 0.08 mmol $YbCl_3$, and 0.02 mmol $ErCl_3$) and 10 mL of aqueous solution of sodium citrate (1 M) were mixed under stirring for 1 h. Sequentially, 20 mL of aqueous solution of NH_4F (1 M) was added into the above mixed solutions. The mixtures were thoroughly stirred for 30 min and then transferred into a 50 mL Teflon-lined autoclave and heated at 200 °C for 8 h. After the reaction, the autoclave was naturally cooled down to room temperature. The as-prepared SrF_2 NCs were collected by centrifugation at 6000 rpm for 4 min, washed with ethanol and deionized water several times, and finally dried at 60 °C for 12 h.

2.2. Characterization. The morphology and size of the as-prepared SrF_2 NCs were characterized by transmission electron microscopy (TEM). X-ray diffraction (XRD) patterns were measured using a powder diffractometer (Bruker D8 Advance) working in a Bragg−Brentano geometry ray with a copper anode X-ray source and a cooled solid-state detector. The visible and NIR luminescence spectra of SrF_2:Nd^{3+}/Yb^{3+}/Er^{3+} NCs were measured using a fluorescence spectrophotometer (Zolix Omni-l3072i) coupled with an R928 photomultiplier tube or an InGaAs avalanche photodetector under the excitation of 808 and 980 nm lasers.

2.3. Metal Ion Detection Studies Using SrF_2:Nd^{3+}/Yb^{3+}/Er^{3+} NCs. Taking the preparation of the Cu^{2+} ion solution (10^{-8} M) as an example, first, 0.5 mL of the

https://doi.org/10.1021/acsomega.2c01968
ACS Omega 2022, 7, 27230−27238

SrF_2:Nd^{3+}/Yb^{3+}/Er^{3+} NC dispersion solution (6 mg mL^{-1}) was mixed with 0.15 mL of the Cu^{2+} ion solution (10^{-7} M). Then, 0.85 mL of anhydrous ethanol was added to the above mixed solutions, keeping the total volume to 1.5 mL. Finally, it was shaken well and set aside for further use. The configuration method of other Cu^{2+} concentrations and metal ion solutions is similar to the above procedure.

2.4. Solid-State Display Studies Using SrF_2:Nd^{3+}/Yb^{3+}/Er^{3+} NCs. For the solid-state display studies, we engraved the different object patterns on the rubber seal. The as-prepared SrF_2:Nd^{3+}/Yb^{3+}/Er^{3+} NCs coated the notch with a shallow layer of epoxy gum. Finally, we evenly and closely sprinkled a layer of the prepared NC powder and dried it before use.

3. RESULTS AND DISCUSSION

3.1. Structure. Figure 1a–e shows the TEM images of SrF_2:Nd^{3+}/Yb^{3+} (15/4 mol %) NCs doped with different concentrations of Er^{3+} ions. It reveals that the prepared NCs are evenly distributed and mainly elliptic or square. Through the statistical analysis, the average size of the particle is approximately ~55 nm, as shown in Figure 1f. The NCs are relatively uniform in size with small deviations. The results indicate that the doping of different concentrations of rare earth ions has little influence on the morphology and size of the SrF_2 NCs.

Figure 2 shows the XRD patterns of the SrF_2:Nd^{3+}/Yb^{3+} (15/4 mol %) NCs doped with different Er^{3+} ion

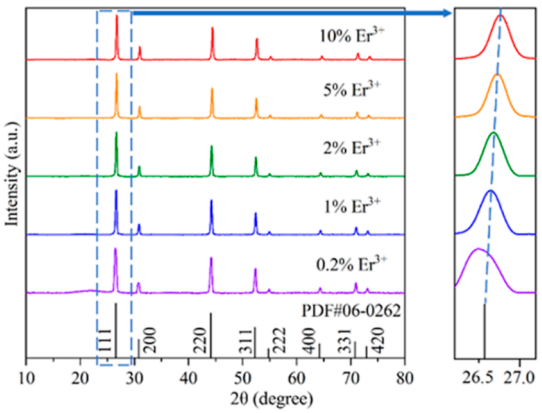

Figure 2. XRD patterns of SrF_2:Nd^{3+}/Yb^{3+}/Er^{3+} (15/4/x mol %) NCs doped with different Er^{3+} ion concentrations.

concentrations. All the measured diffraction peaks of the samples can be well matched to the standard diffraction data of SrF_2 (JCPDS card no. 06-0262), meaning that these as-prepared NCs all crystallize in a cubic structure with a space group of $Fm\bar{3}m$ (225). Nevertheless, as the doping concentrations of Nd^{3+}, Yb^{3+}, and Er^{3+} ions increase, the XRD peak (~26.77°) shifts slightly to a larger degree compared to that of the pure SrF_2. The reason is that the radii of Yb^{3+} (0.86 Å), Nd^{3+} (0.99 Å), and Er^{3+} (0.88 Å) are all smaller than those of the Sr^{2+} ions (1.18 Å). When the bivalent Sr^{2+} ions are replaced by trivalent Yb^{3+} (Nd^{3+} or Er^{3+}) ions, the distance between the lattice planes becomes smaller, thus leading to the diffraction angle increasing according to the Bragg equation.[25] No impurity phase is detected, indicating that the Nd^{3+}, Yb^{3+}, and Er^{3+} tridoped SrF_2 NCs have been successfully synthesized.

3.2. Photoluminescence. Figure 3 shows both UCL and DCL spectra of Nd^{3+}/Yb^{3+}/Er^{3+} tridoped SrF_2 NCs under the dual-wavelength excitation of 808 and 980 nm lasers. Efficient UCL and DCL can be detected. The pumping power intensity is 0.1 W cm^{-2} in our experiments to avoid or minimize the effects of laser-induced heat. Although the UCL and DCL can be efficiently observed at both 808 and 980 nm excitations at the same time, the total emission intensity obtained by an excitation of 808 nm is almost 10 times that by the 980 nm excitation under the same measurement conditions. This is because of the relatively larger absorption cross-section of Nd^{3+} at 808 nm compared to that of Yb^{3+} ions at 980 nm, as previously explained in the Introduction section.

As shown in Figure 3a, under the excitation of an 808 nm laser, typical UCL emissions of Er^{3+} can be clearly observed. The UCL emissions centered at 410, 521, 540, and 652 nm are ascribed to the $^2H_{9/2} \rightarrow {}^4I_{15/2}$, $^4F_{7/2} \rightarrow {}^4I_{15/2}$, $^4S_{3/2} \rightarrow {}^4I_{15/2}$, and $^4F_{9/2} \rightarrow {}^4I_{15/2}$ transition from Er^{3+} ions, respectively. In the NIR DCL spectra shown in Figure 3b, the peaks at 980 nm originate from the $^2F_{5/2} \rightarrow {}^2F_{7/2}$ transitions from Yb^{3+} ions, while the peaks at 867, 1056, and 1330 nm originate from the $^4F_{3/2} \rightarrow {}^4I_{9/2}$, $^4F_{3/2} \rightarrow {}^4I_{11/2}$, and $^4F_{3/2} \rightarrow {}^4I_{13/2}$ transitions from Nd^{3+} ions, respectively. The spectral intensity of the NCs gradually decreases with the increase of Er^{3+} concentration, and 0.2% Er^{3+} is the optimal concentration for achieving the strongest luminescence output. Under the excitation of a 980 nm laser, the shape of the spectra and the concentration-dependent luminescence are the same as those of the NCs excited under 808 nm,[26] as shown in Figure 3c,d.

To clarify the ET mechanism of SrF_2:Nd^{3+}/Yb^{3+}/Er^{3+} NCs excited at 808 and 980 nm, Figure 4 displays the energy level diagram containing the ET processes, excited-state absorption (ESA), cross-relaxation (CR), and NR transition. Under the excitation of 808 nm, when the NCs are codoped with Nd^{3+} and Yb^{3+} ions, Nd^{3+} ions can be populated through the $^4I_{9/2} \rightarrow {}^4F_{5/2}$ transition by absorbing 808 nm photons.[27] Subsequently, the electrons in the $^4F_{3/2}$ state will transition to the $^4I_{9/2}$, $^4I_{11/2}$, and $^4I_{13/2}$ states, thereby emitting the NIR light at 867, 1056, and 1330 nm, respectively. Sectional electrons in the $^4F_{5/2}$ state reach the $^2G_{9/2}$ state by the ESA process and then populate the excited states of $^4G_{7/2}$, $^4G_{5/2}$, and $^4F_{13/2}$ by NR transitions, generating the UCL signals at 542, 586, and 667 nm, respectively. In addition, the $^4F_{5/2}$ state of Nd^{3+} can populate the $^2F_{5/2}$ state of Yb^{3+} through the ET process, thus producing 976 nm NIR DCL. When further introduced with Er^{3+} ions, the Nd^{3+} ions could populate the $^2F_{5/2}$ state of adjacent Yb^{3+} by ET processes and sequentially transfer energy to the $^4I_{11/2}$, $^4F_{7/2}$, and $^2H_{9/2}$ states of Er^{3+} ions through several successive ET processes.[28,29] In addition, besides the population process of $Nd^{3+} \rightarrow Yb^{3+} \rightarrow Er^{3+}$ mentioned above, Nd^{3+} can directly populate the $^4I_{9/2}$ and $^2H_{9/2}$ states of Er^{3+} ions through the ET process ($Nd^{3+} \rightarrow Er^{3+}$) between Nd^{3+} and Yb^{3+} ions. The efficient population of the high-energy states of Er^{3+} can relax them to the corresponding excited states through the NR transition, such as $^2H_{9/2}$, $^2H_{11/2}$, $^4S_{3/2}$, and $^4F_{9/2}$ states, thus generating the UCL centered at 410, 521, 540, and 650 nm, respectively.

Instead of Nd^{3+} ions absorbing 808 nm photons, the Yb^{3+} ions can absorb 980 nm photons directly to make the transition of $^2F_{7/2} \rightarrow {}^2F_{5/2}$.[30,31] On the one hand, Yb^{3+} as the sensitizer will transfer energy to the adjacent Nd^{3+} ions through ET processes, populating the $^2G_{9/2}$ and $^4F_{3/2}$ states of

https://doi.org/10.1021/acsomega.2c01968
ACS Omega 2022, 7, 27230−27238

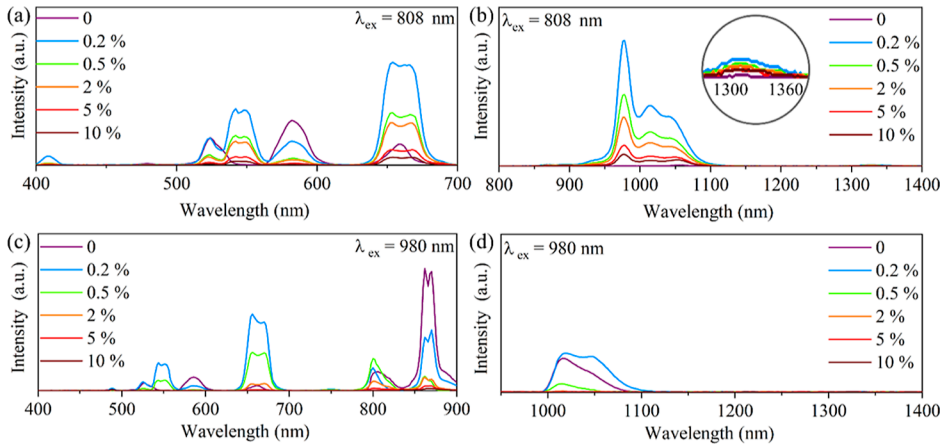

Figure 3. Visible UCL and NIR DCL spectra of SrF_2:Nd^{3+}/Yb^{3+}/Er^{3+} (15/4/x mol %) NCs doped with different Er^{3+} concentrations under the excitation of (a,b) 808 and (c,d) 980 nm, respectively.

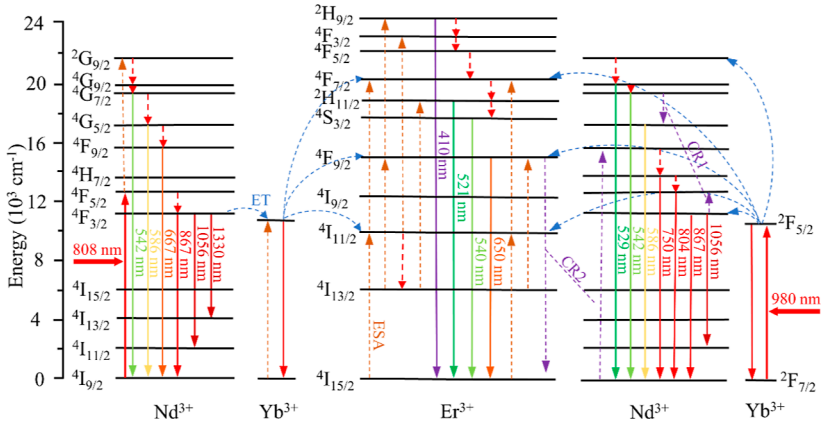

Figure 4. Energy level diagram for SrF_2:Nd^{3+}/Yb^{3+}/Er^{3+} NCs excited at 808 and 980 nm, respectively. The corresponding processes of ET, ESA, and CR; NR transitions; UCL and DCL channels are also provided.

Nd^{3+} ions. Especially, the CR1 process can significantly populate the $^4F_{5/2}$ state. This can efficiently generate the 804 nm UCL compared to pumped at 808 nm laser. In addition, the CR2 process of $^4I_{9/2}$ (Nd^{3+}) + $^4F_{9/2}$ (Er^{3+}) → $^4I_{15/2}$ (Er^{3+}) + $^4F_{9/2}$ (Nd^{3+}) will promote the population of the $^4F_{9/2}$ state of Nd^{3+} and then radiate to the $^4H_{7/2}$ state, achieving the 750 nm ($^4H_{7/2}$ → $^4I_{9/2}$) emission.[32] On the other hand, Yb^{3+} can also transfer energy to Er^{3+} ions by ET processes to populate the $^4I_{11/2}$, $^4F_{9/2}$, $^4F_{7/2}$, and $^2H_{9/2}$ states of Er^{3+}, thus leading to the typical UCL of Er^{3+}.

Figure 5a,c shows the UCL spectra of SrF_2:Nd^{3+}/Yb^{3+}/Er^{3+} (15/4/0.2 mol %) NCs excited by 808 and 980 nm lasers with different pumping power densities. All the UCL intensities increase gradually with the pumping power density. It is well known that the UCL intensity and pumping power density follow the relationship, $I \propto P^n$, that is, the UCL intensity (I) is proportional to the pumping power density (P), and n is the number of photons absorbed for each emitted photon. Figure 5b,d further display the dependence of UCL intensity on the pumping power density. The slope of the fitted curve for 410 nm is greater than 2, indicating that it originates from the three-photon absorption process. The slopes of the other UCL curves are between 1 and 2, revealing that these observed UCLs originate from the two-photon absorption process. The results match well with the discussed UC emission processes in Figure 4.

3.3. Metal Ion Concentration Detection.

Having demonstrated the efficient UCL and DCL of the as-prepared NCs, here, we select the SrF_2:Nd^{3+}/Yb^{3+}/Er^{3+} (15/4/0.2 mol %) NCs as an optical sensor to detect the metal ion. Figure 6a gives the spectra of SrF_2:Nd^{3+}/Yb^{3+}/Er^{3+} (15/4/0.2 mol %) NCs dispersed in different concentrations of Cu^{2+} ion solutions under the excitation of an 808 nm laser. With the increase of Cu^{2+} ion concentrations from 1 to 10 nM, the peak positions of the UCL and DCL remain unchanged. However, both the UCL and DCL gradually decrease when increasing the Cu^{2+} concentrations. The luminescence inhibition effect of the NCs becomes more obvious at relatively high Cu^{2+} concentrations. This is possibly caused by the addition of Cu^{2+} ions which inhibit the process of ET between the rare earth ions doped in the NCs.[33−35] This luminescence quenching effect can be utilized for optical sensor detection of the metal ion concentrations. Generally, the Stern−Volmer equation is used to describe the photoluminescence quenching process (dynamic/static), which is defined as follows[36]

$$I_0/I = 1 + K_{SV} \times [Q] \quad (1)$$

where I_0 and I represent the luminescence intensity in the absence and presence of Cu^{2+} ions, respectively, K_{SV} is the dynamic quenching constant (Stern−Volmer quenching constant), and Q is the Cu^{2+} concentration of the solution. Based on the spectral data in Figure 6a, we have calculated the

https://doi.org/10.1021/acsomega.2c01968
ACS Omega 2022, 7, 27230−27238

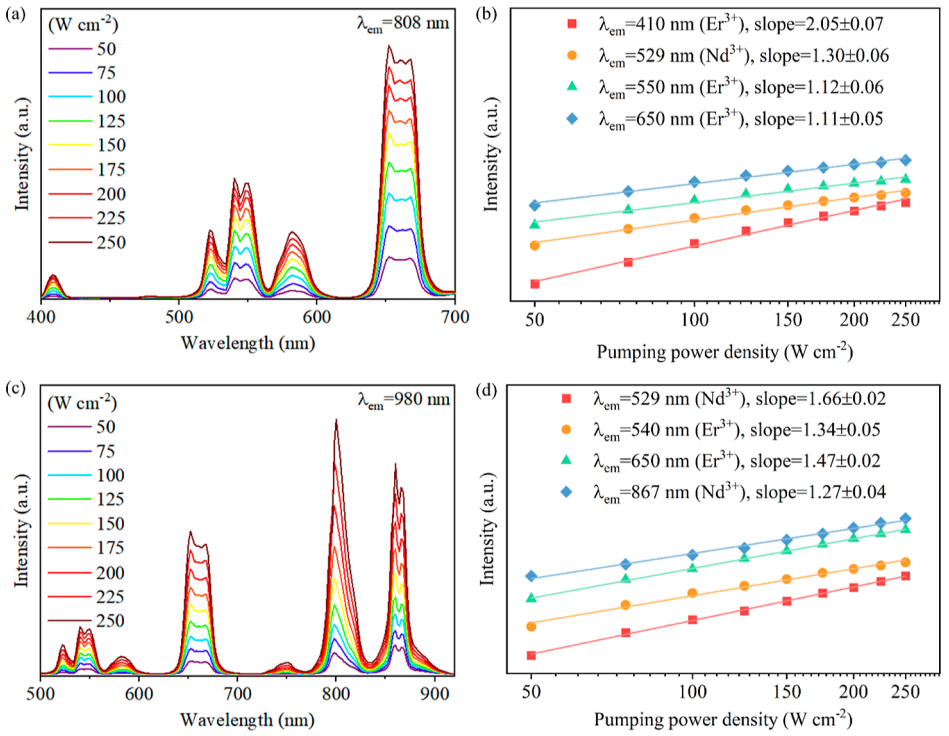

Figure 5. Spectra of SrF_2:Nd^{3+}/Yb^{3+}/Er^{3+} (15/4/0.2 mol %) NCs excited by (a) 808 and (c) 980 nm lasers with different pumping power densities. Double-logarithmic plots of luminescent intensity vs different pumping power densities under (b) 808 and (d) 980 nm.

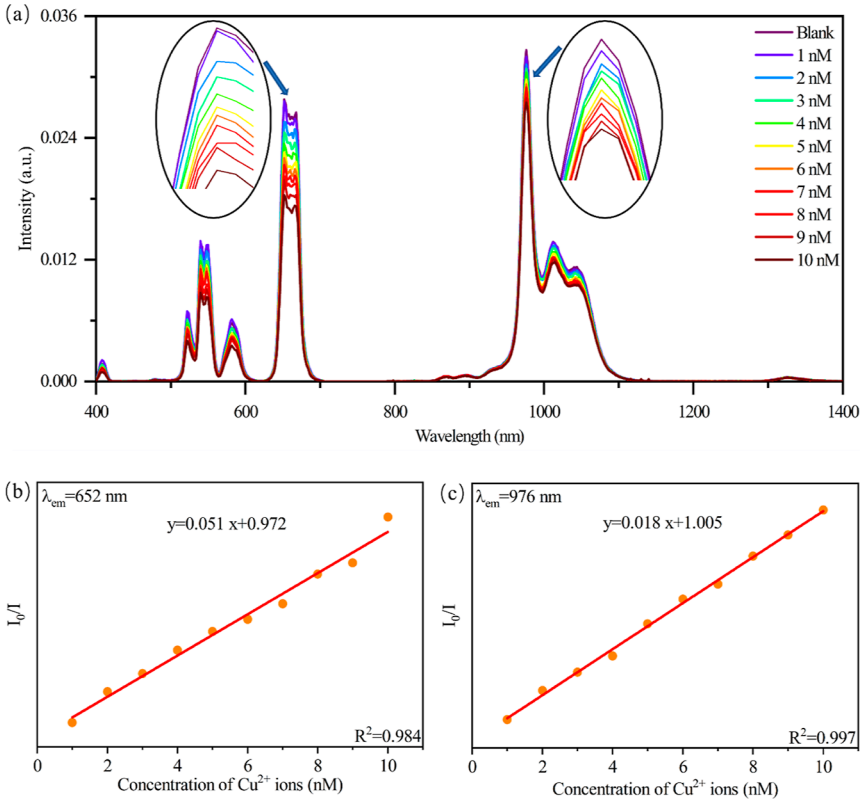

Figure 6. (a) DCL and UCL intensity of SrF_2:Nd^{3+}/Yb^{3+}/Er^{3+} (15/4/0.2 mol %) NCs as a function of the Cu^{2+} ion concentrations. The Stern−Volmer plot as a function of Cu^{2+} concentration for SrF_2:Nd^{3+}/Yb^{3+}/Er^{3+} (15/4/0.2 mol %) NCs measured at (b) visible UCL (652 nm) and (c) NIR DCL (976 nm), respectively. The excitation wavelength is 808 nm.

ratios of 652 nm visible emission and 976 nm NIR light. Figure 6b,c shows the corresponding Stern−Volmer plots as a function of the Cu^{2+} concentrations. According to the plot, a linear relationship can be obtained between the luminescence ratio and the Cu^{2+} ion concentration for both 652 nm (R^2 = 0.984) and 976 nm (R^2 = 0.997). The limit of detection

https://doi.org/10.1021/acsomega.2c01968
ACS Omega 2022, 7, 27230−27238

Table 1. LOD and Linearity Range Comparison of Various Samples Applied for the Detection of Cu^{2+} Ions

samples	λ_{ex} (nm)	λ_{em} (nm)	concentration detection range	LOD	reference
$CuInS_2/ZnS$	450	695	75−750 nM	63 nM	21
$Cit/CaF_2:Ce^{3+}/Tb^{3+}$	302	543	2−20 μM	10.2 μM	23
$SrF_2:Ce^{3+}/Tb^{3+}$	290	544	1−10 nM	2.2 nM	36
$CdTe/Fe_3O_4$	400	575	2−800 μM	1.8 μM	39
$KZnF_3:Eu^{3+}$	394	614	10−100 μM	0.48 μM	40
$BaF_2:Ce^{3+}/Tb^{3+}$	287	545	20−100 μM		41
$SrF_2:Nd^{3+}/Yb^{3+}/Er^{3+}$	808	652	1−10 nM	0.22 nM	this work
$SrF_2:Nd^{3+}/Yb^{3+}/Er^{3+}$	808	976	1−10 nM	0.63 nM	this work

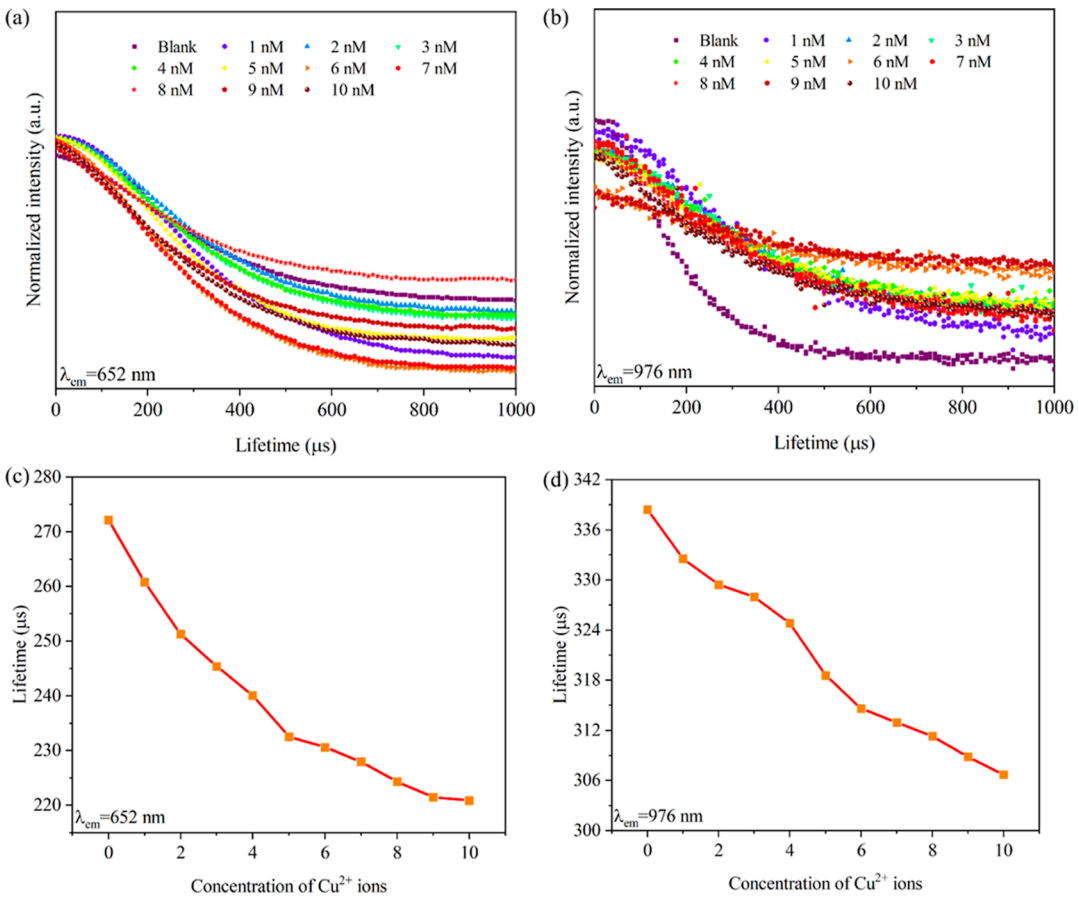

Figure 7. Lifetime of $SrF_2:Nd^{3+}/Yb^{3+}/Er^{3+}$ (15/4/0.2 mol %) NCs dispersed in different concentrations of Cu^{2+} ions at the (a) visible UCL (652 nm) and (b) NIR DCL (976 nm). Dependence of (c) visible UCL (652 nm) and (d) NIR DCL (976 nm) lifetimes of $SrF_2:Nd^{3+}/Yb^{3+}/Er^{3+}$ (15/4/0.2 mol %) NCs on the Cu^{2+} ion concentrations. The excitation wavelengths are all 808 nm.

(LOD) can be further calculated using the following formula[37,38]

$$\mathrm{LOD} = 3\sigma/S \quad (2)$$

where σ is the standard deviation of the blank experiment and S is the slope of the calibration plot. In our measurements, σ is about 3.77×10^{-4}, which is calculated after several measurements of the original sample without Cu^{2+} ion doping. According to the obtained parameters, the detection limit value was therefore calculated to be 0.22 nM (652 nm) and 0.63 nM (976 nm), respectively. This probed value is extremely higher than the maximum Cu^{2+} ion concentration (~31.5 μM) permitted in drinking water given by the WHO.[20] Therefore, these NCs can be applied for detecting the Cu^{2+} ions in the drinking water for quality monitoring. Compared with other NCs, these NCs have a better detection accuracy for Cu^{2+} ion concentration detection, which is summarized in Table 1.

Figure 7a,b displays the decay curve of the emission peak at 652 and 976 nm with changing the Cu^{2+} concentrations from 1 to 10 nM in the $SrF_2:Nd^{3+}/Yb^{3+}/Er^{3+}$ NC sample under 808 nm excitation. Meanwhile, to clearly compare the lifetime variations, Figure 7c,d further shows the dependence of both the visible UCL and NIR DCL lifetimes on the Cu^{2+} concentrations. A single exponential function has been used to fit the lifetime of the fluorescence decay curves. It can be seen that both the lifetimes of 652 and 976 nm gradually decrease with the increase of Cu^{2+} concentrations. The lifetime of the transition $^4F_{9/2} \rightarrow {}^4I_{15/2}$ (652 nm) of Er^{3+} ions drops from 275.15 to 220.89 μs as well as that of the transition $^2F_{5/2} \rightarrow {}^2F_{7/2}$ (976 nm) of Yb^{3+} ions decreases from 338.43 to 306.72 μs.

https://doi.org/10.1021/acsomega.2c01968
ACS Omega 2022, 7, 27230−27238

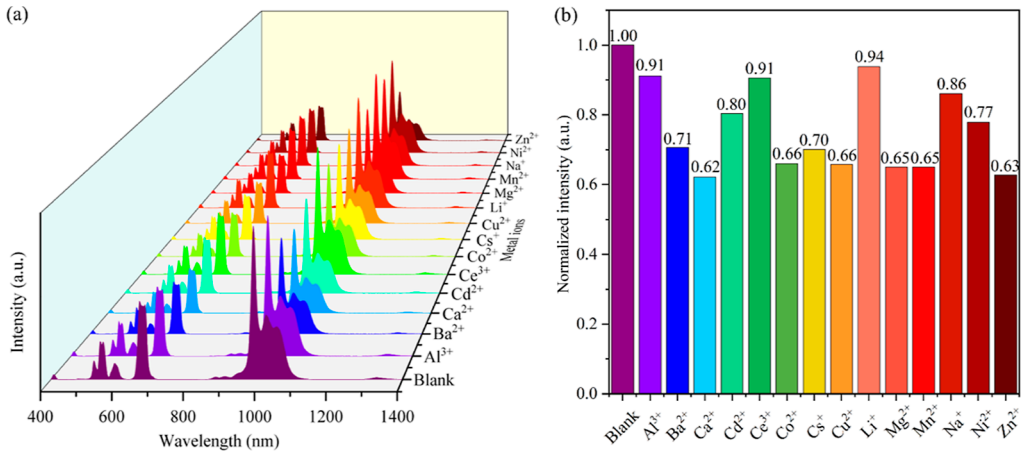

Figure 8. (a) Spectra of SrF_2:Nd^{3+}/Yb^{3+}/Er^{3+} (15/4/0.2 mol %) NCs dispersed in different metal ions with the same concentration (10 nM) excited under an 808 nm laser. (b) Normalized spectral intensity of different kinds of metal ions (the luminescence intensity for the NCs without any metal ion is normalized as the reference value "1").

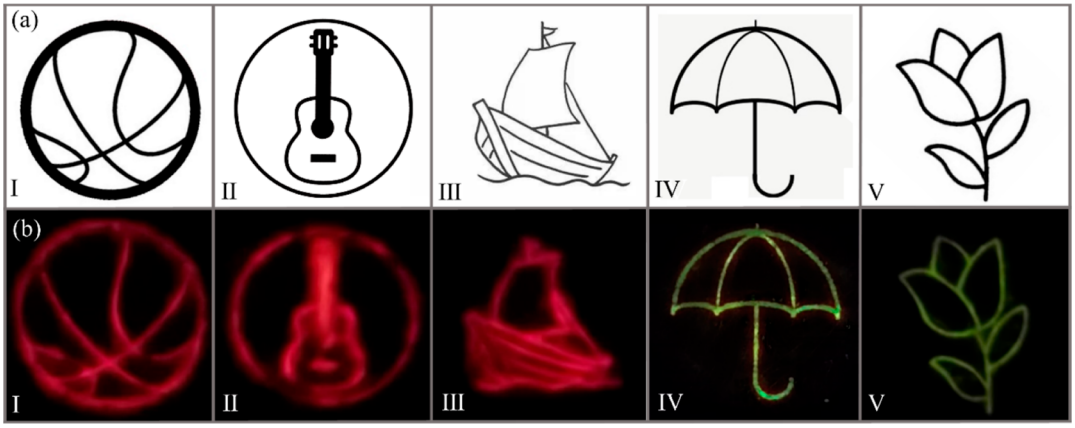

Figure 9. (a) Original pictures of a basketball (I), guitar (II), sailboat (III), umbrella (IV), and flower (V). (b) Displayed "red" and "green" patterns drawn with the prepared SrF_2 NCs doped with different Nd^{3+}, Yb^{3+}, and Er^{3+} ions under 980 nm laser illumination. The drawn NCs are (I) SrF_2:Nd^{3+}/Yb^{3+}/Er^{3+} (15/4/0.5 mol %), (II) SrF_2:Nd^{3+}/Yb^{3+}/Er^{3+} (15/4/1 mol %), (III) SrF_2:Nd^{3+}/Yb^{3+}/Er^{3+} (15/4/2 mol %), (IV) SrF_2:Nd^{3+}/Yb^{3+}/Er^{3+} (15/4/10 mol %), and (V) SrF_2:Nd^{3+}/Yb^{3+}/Er^{3+} (10/2/1 mol %).

After investigating the detection of Cu^{2+} ion concentrations, we tried to detect other metal ions. Figure 8a shows the emission spectra of SrF_2:Nd^{3+}/Yb^{3+}/Er^{3+} NCs dispersed in solutions with different kinds of metal ions at the same concentrations (10 nM) under 808 nm excitation. To clearly quantitatively determine the influence of various metal ions on the luminescence property, the emission intensity of the sample without any metal ion is taken as the reference value "1", as shown in Figure 8b. The results manifest that Li^+ ions have the least inhibitory effect on the UCL and DCL, while Ca^{2+} and Zn^{2+} ions have the strongest quenching effects. Generally, numerous efforts have been made to detect metal ions, including atomic absorption spectroscopy, electrochemical sensing, X-ray fluorescence, and optical spectroscopy detection. The possible quenching principle and explanation, such as the photoinduced electron transfer, intramolecular charge transfer, and fluorescence resonance ET, have also been widely discussed in some previous reports.[42−45]

3.4. Solid-State Imaging Display. To further visualize the emission spectra of our samples and expand the application of the NCs in solid-state imaging displays and anti-counterfeiting identification, we used the NC embedding in the engraving vivid pictures under 980 nm excitation, as shown in Figure 9. Picture I (basketball) is drawn with SrF_2:Nd^{3+}/Yb^{3+}/Er^{3+} (15/4/0.5 mol %) NCs. It is noted that the excitation of different samples under the same wavelength laser can get different imaging colors. Bright and clear "red" patterns can be observed in pictures I (basketball), II (guitar), and III (sailboat) achieved with the SrF_2:Nd^{3+}/Yb^{3+}/Er^{3+} (15/4/0.5 mol %), SrF_2:Nd^{3+}/Yb^{3+}/Er^{3+} (15/4/1 mol %), and SrF_2:Nd^{3+}/Yb^{3+}/Er^{3+} (15/4/2 mol %) NCs, respectively. Moreover, "green" patterns can be detected in pictures IV (umbrella) and V (flowers) when sealed with SrF_2:Nd^{3+}/Yb^{3+}/Er^{3+} (15/4/10 mol %) and SrF_2:Nd^{3+}/Yb^{3+}/Er^{3+} (10/2/1 mol %) NCs. Therefore, we fully believe that a specific color light output can be achieved through doping with different Nd^{3+}, Yb^{3+}, and Er^{3+} concentrations, which will greatly promote the development of solid-state display research.

4. CONCLUSIONS

In summary, we have fabricated the Nd^{3+}, Yb^{3+}, and Er^{3+} tridoped SrF_2 NCs with an average size of 55 nm by a hydrothermal method. Subsequently, their NIR DCL and visible UCL properties are systematically characterized under dual-wavelength excitation (both 808 and 980 nm lasers). The results verify that these NCs can simultaneously efficiently

https://doi.org/10.1021/acsomega.2c01968
ACS Omega 2022, 7, 27230−27238

exhibit both the NIR DCL and UCL signals. Based on the spectra under dual-wavelength excitation, the mechanism of the DCL and UCL and populations of these SrF_2:Nd^{3+}/Yb^{3+}/Er^{3+} NCs are demonstrated. Furthermore, the SrF_2:Nd^{3+}/Yb^{3+}/Er^{3+} (15/4/0.2 mol %) NCs are further utilized for detecting the Cu^{2+} ions, and the probe accuracy is on the nanomolar concentration scale (0.22 nM at 652 and 0.63 nM at 976 nm). It also reveals that these NCs can be applied for detection of other common metal ion concentration. In addition, we embedded the NCs doped with different Nd^{3+}, Yb^{3+}, and Er^{3+} ions into the engraving structure pictures and achieved obvious "red" and "green" patterns for a solid-state imaging display. We firmly believe that these NCs have great potential applications in the detection of metal ion concentration and solid-state displays.

AUTHOR INFORMATION

Corresponding Authors

Maohui Yuan − *College of Advanced Interdisciplinary Studies and State Key Laboratory of Pulsed Power Laser Technology, National University of Defense Technology, Changsha 410073, China;* orcid.org/0000-0002-4952-4417; Email: yuanmaohuino1@126.com

Hongyan Wang − *College of Advanced Interdisciplinary Studies, State Key Laboratory of Pulsed Power Laser Technology, and Hunan Provincial Key Laboratory of High Energy Laser Technology, National University of Defense Technology, Changsha 410073, China;* Email: wanghongyan@nudt.edu.cn

Authors

Linxuan Wang − *College of Advanced Interdisciplinary Studies and State Key Laboratory of Pulsed Power Laser Technology, National University of Defense Technology, Changsha 410073, China*

Weiqiang Yang − *College of Advanced Interdisciplinary Studies, National University of Defense Technology, Changsha 410073, China; Institute of Optics and Electronics and Key Laboratory of Optical Engineering, Chinese Academy of Sciences, Chengdu 610209, China; University of Chinese Academy of Sciences, Beijing 100049, China*

Liang Li − *College of Advanced Interdisciplinary Studies and State Key Laboratory of Pulsed Power Laser Technology, National University of Defense Technology, Changsha 410073, China*

Shuai Hu − *College of Advanced Interdisciplinary Studies and State Key Laboratory of Pulsed Power Laser Technology, National University of Defense Technology, Changsha 410073, China*

Zining Yang − *College of Advanced Interdisciplinary Studies, State Key Laboratory of Pulsed Power Laser Technology, and Hunan Provincial Key Laboratory of High Energy Laser Technology, National University of Defense Technology, Changsha 410073, China*

Kai Han − *College of Advanced Interdisciplinary Studies, State Key Laboratory of Pulsed Power Laser Technology, and Hunan Provincial Key Laboratory of High Energy Laser Technology, National University of Defense Technology, Changsha 410073, China;* orcid.org/0000-0001-7689-5339

Xiaojun Xu − *College of Advanced Interdisciplinary Studies, State Key Laboratory of Pulsed Power Laser Technology, and Hunan Provincial Key Laboratory of High Energy Laser Technology, National University of Defense Technology, Changsha 410073, China*

Complete contact information is available at: https://pubs.acs.org/10.1021/acsomega.2c01968

Author Contributions

[¶]L.W. and W.Y. contributed equally to this work.

Notes

The authors declare no competing financial interest.

REFERENCES

(1) Zhou, J.; Lei, R. S.; Wang, H. P.; Chen, C.; Chen, B. W.; Pan, E.; Zhao, S. L.; Xu, S. Q. Er^{3+}/Yb^{3+}-codoped ZrO_2 nanocrystals as ratiometric luminescence nanothermometers that cover three biological windows. *ACS Appl. Nano Mater.* **2020**, *3*, 186−194.

(2) Yun, R.; He, J. Q.; Luo, L.; Liu, X. H.; Nie, Z. G.; Zhao, W. R.; Wen, H. L. Upconversion luminescence and temperature sensing properties in $LiGd(WO_4)_2$: Er^{3+}, Yb^{3+}, Nd^{3+} microparticles under 785 excitation. *Ceram. Int.* **2021**, *47*, 16062−16069.

(3) Wu, X. F.; Zhan, S. P.; Han, J. B.; Liu, Y. X. Nanoscale ultrasensitive temperature sensing based on upconversion nanoparticles with lattice self-adaptation. *Nano Lett.* **2021**, *21*, 272−278.

(4) Wei, Z. W.; Sun, L. N.; Liu, J. L.; Zhang, J. Z.; Yang, H. R.; Yang, Y.; Shi, L. Y. Cysteine modified rare-earth up-converting nanoparticles for in vitro and in vivo bioimaging. *Biomaterials* **2014**, *35*, 387−392.

(5) Ouyang, T. C.; Kang, S. L.; Zhang, Z. S.; Yang, D. D.; Huang, X. J.; Pan, Q. W.; Gan, J. L.; Qiu, J. R.; Dong, G. P. Microlaser output from rare-earth ion-doped nanocrystal-in-glass microcavities. *Adv. Opt. Mater.* **2019**, *7*, 1900197.

(6) Fernandez-Bravo, A.; Yao, K. Y.; Barnard, E. S.; Borys, N. J.; Levy, E. S.; Tian, B. N.; Tajon, C. A.; Moretti, L.; Altoe, M. V.; Aloni, S.; Beketayev, K.; Scotognella, F.; Cohen, B. E.; Chan, E. M.; Schuck, P. J. Continuous-wave upconverting nanoparticle microlasers. *Nat. Nanotechnol.* **2018**, *13*, 572−577.

(7) Ding, M. Y.; Ni, Y.; Song, Y.; Liu, X.; Cui, T.; Chen, D.; Ji, Z.; Xu, F.; Lu, C.; Xu, Z. Li^+ ions doping core-shell nanostructures: an approach to significantly enhance upconversion luminescence of lanthanide-doped nanocrystals. *J. Alloys Compd.* **2015**, *623*, 42−48.

(8) Vellampatti, S.; Reddeppa, M.; Dugasani, S. R.; Mitta, S. B.; Gnapareddy, B.; Kim, M. D.; Park, S. H. High performance UV photodetectors using Nd^{3+} and Er^{3+} single- and co-doped DNA thin films. *Biosens. Bioelectron.* **2019**, *126*, 44−50.

(9) You, M.; Zhong, J.; Hong, Y.; Duan, Z.; Lin, M.; Xu, F. Inkjet printing of upconversion nanoparticles for anti-counterfeit applications. *Nanoscale* **2015**, *7*, 4423−4431.

(10) Shi, Z.; Duan, Y.; Zhu, X. J.; Wang, Q. W.; Li, D. D.; Hu, K.; Feng, W.; LiXu, F. Y. C. X. Dual functional $NaYF_4$:Yb^{3+}, Er^{3+}@$NaYF_4$:Yb^{3+}, Nd^{3+} core−shell nanoparticles for cell temperature sensing and imaging. *Nanotechnology* **2017**, *29*, 094001.

(11) Zhou, Z. W.; Li, W. W.; Song, J. H.; Yi, G. Q.; Mei, B. C.; Su, L. B. Synthesis and characterization of Nd^{3+} doped SrF_2 nanoparticles prepared by precipitation method. *Ceram. Int.* **2018**, *44*, 4344−4350.

(12) Du, S.; Wang, Y. A broad-range temperature sensor depend on the magnetic and optical properties of SrF_2:Yb^{3+}, Ho^{3+}. *CrystEngComm* **2019**, *21*, 1452−1457.

(13) Marciniak, L.; Bednarkiewicz, A.; Elzbieciak, K. NIR-NIR photon avalanche based luminescent thermometry with Nd^{3+} doped nanoparticles. *J. Mater. Chem. C* **2018**, *6*, 7568−7575.

(14) Song, H. L.; Han, Q.; Tang, X. Y.; Zhao, X. R.; Ren, K.; Liu, T. G. Nd^{3+}/Yb^{3+} codoped $SrWO_4$ for highly sensitive optical thermometry based on the near infrared emission. *Opt. Mater.* **2018**, *84*, 263−267.

(15) Cortelletti, P.; Pedroni, M.; Boschi, F.; Pin, S.; Ghigna, P.; Canton, P.; Vetrone, F.; Speghini, A. Luminescence of Eu^{3+} activated CaF_2 and SrF_2 nanoparticles: effect of the particle size and codoping with alkaline ions. *Cryst. Growth Des.* **2018**, *18*, 686−694.

https://doi.org/10.1021/acsomega.2c01968
ACS Omega 2022, 7, 27230−27238

(16) Hernández-Rodríguez, M. A.; Lozano-Gorrína, A. D.; Martína, I. R.; Rodríguez-Mendoza, U. R.; Lavín, V. Comparison of the sensitivity as optical temperature sensor of nano-perovskite doped with Nd^{3+} ions in the first and second biological windows. *Sens. Actuators, B* **2018**, *255*, 970−976.
(17) Ma, X. Y.; Bai, Z. H.; Liu, Z. Y.; Zhang, Y. Z.; Cui, J. Luminescence properties of PbF_2:Nd^{3+}, Er^{3+}, Yb^{3+} phosphors and it's multi-wavelength sensitive bidirectional conversion mechanism. *J. Alloys Compd.* **2020**, *824*, 153898.
(18) Mare, S.; Penugonda, S.; Robinson, S. M.; Dohgu, S.; Banks, W. A.; Ercal, N. Copper complexing decreases the ability of amyloid beta peptide to cross the BBB and enter brain parenchyma. *Peptides* **2007**, *28*, 1424−1432.
(19) Poujois, A.; Woimant, F. Wilson's disease: a 2017 update. *Clin. Res. Hepatol. Gastroenterol.* **2018**, *42*, 512−520.
(20) Pirrone, N.; Mahaffey, K. R. *Dynamics of mercury pollution on regional and global scales: atmospheric processes and human exposures around the world*; Springer, 2005.
(21) Rajendran, J. V.; Parani, S.; Pillay R Remya, V. P. R.; Lebepe, T. C.; Maluleke, R.; Thomas, S.; Oluwafemi, O. S. Selective and sensitive detection of Cu^{2+} ions in the midst of other metal ions using glutathione capped $CuInS_2$/ZnS quantum dots. *Physica E* **2022**, *136*, 115026.
(22) Wong, Y. T.; Pang, S. Y.; Tsang, M. K.; Liu, Y.; Huang, H. T.; Yu, S. F.; Hao, J. H. Electrochemically assisted flexible lanthanide upconversion luminescence sensing of heavy metal contamination with high sensitivity and selectivity. *Nanoscale Adv.* **2019**, *1*, 265−272.
(23) Song, L. M.; Gao, J. H.; Wang, X.; Li, J. T.; Chen, M. X. Highly luminescent Cit/CaF_2: Ce^{3+}, Tb^{3+} nanoparticles and detection of Cu^{2+} ions. *J. Lumin.* **2020**, *226*, 117445.
(24) Wang, L. X.; Yang, X.; Yuan, M. H.; Yang, Z. N.; Han, K.; Wang, H. Y.; Xu, X. J. Determination of near-infrared down-conversion emission of Yb^{3+} and optical temperature sensing performances in Nd^{3+}-sensitized SrF_2 nanocrystals. *Opt. Mater.* **2022**, *123*, 111823.
(25) Li, G.; Shi, S.; Gao, Y.; Zhu, D.; Su, Z. M. Synthesis, characterization of mechanochromic luminescent-active mono-/dinuclear iridium (III) complexes with near-infrared emission. *J. Organomet. Chem.* **2021**, *931*, 121628.
(26) Shang, F. K.; Hu, C. H.; Xu, W.; Zhu, X.; Zhao, D.; Zhang, W. B.; Zhang, Z. G.; Cao, W. W. Near-infrared emitting Nd^{3+}-Yb^{3+} codoped Y_2O_3 nanocrystals for highly sensitive optical thermometry. *J. Alloys Compd.* **2021**, *858*, 157637.
(27) Soni, A. K.; Rai, V. K.; Kumar, S. Cooling in Er^{3+}: $BaMoO_4$ phosphor on codoping with Yb^{3+} for elevated temperature sensing. *Sensor. Actuator. B Chem.* **2016**, *229*, 476−482.
(28) Ye, Z. Q.; Xiao, S.; Yang, X. L. Up-conversion of Nd^{3+}/Yb^{3+}/Tm^{3+} tri-doped $CaTeO_3$ compound under excitation of 808 nm. *Rare Met.* **2021**, *40*, 1008−1013.
(29) Liang, Y.; Shen, L. H.; Wei, T.; Zhao, C. Z.; Jia, B.; Shi, Y.; Wu, S. C. Multi-function up-conversion luminescent $Bi_4Ti_3O_{12}$ nanoparticles sensitized by Nd^{3+} and Yb^{3+}. *Opt. Mater.* **2020**, *109*, 110408.
(30) Bao, Y. N.; Zhang, Z. Y.; Cao, B. S.; Liu, Y.; Shang, J. Y.; Yang, Y.; Dong, B. Energy transfer from Er to Nd ions by the thermal effect and promotion of the photocatalysis of the $NaYF_4$:Yb,Er,Nd/$W_{18}O_{49}$ heterostructure. *Nanoscale* **2019**, *11*, 7433−7439.
(31) Mikalauskaite, I.; Pleckaityte, G.; Sinusaite, L.; Plausinaitiene, V.; Katelnikovas, A.; Beganskiene, A. Temperature induced emission enhancement and investigation of Nd^{3+}→Yb^{3+} energy transfer efficiency in $NaGdF_4$:Nd^{3+}, Yb^{3+}, Er^{3+} upconverting nanoparticles. *J. Lumin.* **2020**, *223*, 117237.
(32) Wang, X.; Xu, T.; Cai, P.; Vu, T.; Seo, H. J. Controlled synthesis, multicolor luminescence, and optical thermometer of bifunctional $NaYbF_4$:Nd^{3+}@$NaYF_4$:Yb^{3+} active-core/active-shell colloidal nanoparticles. *J. Alloys Compd.* **2017**, *691*, 530−536.
(33) Zhao, X. F.; Yang, Z. N.; Yang, X.; Wang, R.; Yuan, M. H.; Han, K.; Jiang, Z. F.; Wang, H. Y.; Xu, X. J. Controlling the multicolor upconversion luminescence in CaF_2 nanocrystals doped with Yb^{3+}, Er^{3+} and Nd^{3+} ions under the excitation of a 808 nm laser. *Opt. Mater. Express* **2019**, *9*, 4578−4587.
(34) Bai, H. Y.; Tu, Z. Q.; Liu, Y. T.; Tai, Q. X.; Guo, Z. K.; Liu, S. Y. Dual-emission carbon dots-stabilized copper nanoclusters for ratiometric and visual detection of $Cr_2O_7^{2-}$ ions and Cd^{2+} ions. *J. Hazard. Mater.* **2020**, *386*, 121654.
(35) Lin, L. Y.; Hu, Y. F.; Zhang, L. L.; Huang, Y.; Zhao, S. L. Photoluminescence light-up detection of zinc ion and imaging in living cells based on the aggregation induced emission enhancement of glutathione capped copper nanoclusters. *Biosens. Bioelectron.* **2017**, *94*, 523−529.
(36) Jalili, R.; Khataee, A. Aluminum(III) triggered aggregation-induced emission of glutathione-capped copper nanoclusters as a fluorescent probe for creatinine. *Microchim. Acta* **2018**, *186*, 29.
(37) Sarkar, S.; Manjunath, C.; Venkata, N. K. B. A.; Venkataramanan, M. Highly selective and sensitive detection of Cu^{2+} ions using Ce(III)/Tb(III)-doped SrF_2 nanocrystals as fluorescent probe. *ACS Appl. Mater. Interfaces* **2015**, *7*, 25702−25708.
(38) Jannetto, P. J. Therapeutic drug monitoring using mass spectrometry in mass spectrum. *Clin. Chem.* **2017**, 165−179.
(39) Huang, L. N.; Chen, F.; Zong, X.; Lu, Q. J.; Wu, C. Y.; Ni, Z. Q.; Liu, M. L.; Zhang, Y. Y. Near-infrared light excited UCNP-DNAzyme nanosensor for selective detection of Pb^{2+} and in vivo imaging. *Talanta* **2021**, *227*, 122156.
(40) Han, J.; Zhang, X.; Zhou, Y.; Ning, Y.; Wu, J.; Liang, S.; Sun, H.; Zhang, H.; Yang, B. Fabrication of CdTe nanoparticles-based superparticles for an improved detection of Cu^{2+} and Ag^{+}. *J. Mater. Chem.* **2012**, *22*, 2679−2686.
(41) Sarkar, S.; Manjunath, C.; Venkataramanan, M. Highly luminescent colloidal Eu^{3+}-doped $KZnF_3$ nanoparticles for the selective and sensitive detection of Cu^{2+} ions. *Chem.—Eur. J.* **2014**, *20*, 3311−3316.
(42) He, W. X.; Du, H. L.; Fu, J.; Luan, F. F.; Li, D. W.; Sun, L. Y.; Guo, D. C. Efficient energy transfer from Ce^{3+} to Tb^{3+} in BaF_2: green-emitting phosphors for potential applications in the detection of Cu^{2+} ions. *New J. Chem.* **2021**, *45*, 1446.
(43) He, G. J.; Zhao, X. W.; Zhang, X. L.; Fan, H. J.; Wu, S.; Li, H. Q.; He, C.; Duan, C. Y. A turn-on PET fluorescence sensor for imaging Cu^{2+} in living cells. *New J. Chem.* **2010**, *34*, 1055−1058.
(44) Hu, J. W.; Hu, Z. J.; Liu, S.; Zhang, Q.; Gao, H. W.; Uvdal, K. A new ratiometric fluorescent chemodosimeter based on an ICT modulation for the detection of Hg^{2+}. *Sens. Actuators, B* **2016**, *230*, 639−644.
(45) Yuan, X.; Leng, T. H.; Guo, Z. Q.; Wang, C. Y.; Li, J. Z.; Yang, W. W.; Zhu, W. H. A FRET-based dual-channel turn-on fluorescence probe for the detection of Hg^{2+} in living cells. *Dyes Pigments* **2019**, *161*, 403−410.

https://doi.org/10.1021/acsomega.2c01968
ACS Omega 2022, 7, 27230−27238